

# A DAMAGE PARTICLE METHOD FOR SMEARED MODELING OF BRITTLE FRACTURE

*Haoyan Wei & Jiun-Shyan Chen\**

*Department of Structural Engineering, University of California, San Diego, La Jolla, CA, USA*

\*Address all correspondence to: Jiun-Shyan Chen, Department of Structural Engineering, University of California, San Diego, La Jolla, CA, USA, E-mail: js-chen@ucsd.edu

*Original Manuscript Submitted: 4/2/2018; Final Draft Received: 6/6/2018*

*Numerical procedures for brittle fracture modeling become tedious when many moving strong discontinuities have to be captured. A smeared fracture modeling approach formulated under the reproducing kernel particle discretization is presented. In this approach, the smeared strain is computed by the divergence operation with a boundary integral of displacements in each nodal representative domain, thus avoiding direct derivatives of displacements for strain computation in the smeared cracking region. To avoid discretization size sensitivity issues, a scaling law is introduced based on the equivalence between the bulk damage energy dissipation and the surface fracture energy of the associated crack segment over the nodal representative domain. This scaling law is introduced under the stabilized conforming nodal integration framework, where the nodal representative domain serves as the smearing domain, and the smeared strain over the nodal representative domain is used with the scaled damage law to determine the damage state. The employment of stabilized conforming nodal integration also allows the displacement and damage state variables to be calculated and stored for the same set of particles, avoiding interpolation of variables between nodal and Gaussian points in conventional finite elements. Several numerical examples are presented to examine the effectiveness of the proposed damage particle method for smeared modeling of fracture.*

**KEY WORDS:** *smeared strain, stabilized conforming nodal integration, reproducing kernel particle method, smeared crack model, continuum damage model*

## 1. INTRODUCTION

In recent years, considerable advances have been made in fracture modeling methods. The first type of methods are the discrete crack approaches in conjunction with adaptive re-meshing (Swenson and Ingraffea, 1988; Rangarajan et al., 2015), interface element insertion (Xu and Needleman, 1994; Truster, 2016), embedded strong discontinuity (Belytschko et al., 1988; Simo et al., 1993; Jirásek, 2000; Oliver et al., 2014), partition of unity-based enrichment (Belytschko and Black, 1999; Moës et al., 1999; Bordas et al., 2008), and visibility/diffraction criterion (Organ et al., 1996; Krysl and Belytschko, 1999). Alternative methods are formulated based on the smeared crack approaches using fixed and rotated crack models (Jirásek and Zimmermann, 1998; Weihe et al., 1998), continuum damage models (Pijaudier-Cabot and Bažant, 1987; Bažant and Pijaudier-Cabot, 1988; de Vree et al., 1995; Peerlings et al., 1996; de Borst, 2002; Cervera and Chiumenti, 2006a,b; Jirásek and Bauer, 2012; de Borst and Verhoosel, 2016), and phase field models (Miehe et al., 2010; Borden et al., 2014; Ambati et al., 2015), to name a few. Nevertheless, modeling a large set of evolving fractures with complicated crack patterns remains challenging.

The discrete crack approaches usually consider continuous crack surfaces, and represent the crack path by using level sets (Moës et al., 2002; Gravouil et al., 2002) or other surface tracking techniques (Oliver et al., 2014; Jäger et al., 2008; Parvaneh and Foster, 2016). However, fracture surfaces in quasi-brittle geomaterials are typically discrete and non-smooth, and can evolve into irregular patterns such as crack branching and merging, making surface tracking techniques ineffective. By relaxing the crack path continuity requirement, alternative methods have been developed with the goal to model complicated fracture phenomena in a simplified way. For instance, inter-element separation

and cohesive interface element methods (Xu and Needleman, 1994) offer flexibility in modeling crack growth along arbitrary finite element edges without any surface tracking procedures. However, the predicted crack patterns of these methods can be sensitive to the shape and orientation of the adopted finite element mesh. In the cracking particle method (CPM) (Rabczuk and Belytschko, 2004), a set of crack segments located at nodal positions are used to describe the overall fracture surfaces. The simplicity and effectiveness of this idea has been studied in both the finite element method (FEM) (Remmers et al., 2003; de Borst et al., 2004, 2006; Song and Belytschko, 2009) and element-free Galerkin (EFG) method (Rabczuk and Belytschko, 2004, 2007; Rabczuk et al., 2010; Rabczuk, 2013), although the latter meshfree discretization is more suitable for particle-based crack models. Nevertheless, similar to other discrete crack models, the strong discontinuities introduced at the cracked particles require subdividing quadrature cells associated with crack segments, modifying the mesh topology or nodal neighbor list, or adding additional nodal degrees of freedom, leading to a greater degree of computational complexity.

Another type of fracture modeling introduces smearing of the sharp discontinuities over a finite domain, and the cracking effects are represented through a softening stress–strain law; these approaches are generally called smeared crack models (Weihe et al., 1998; de Borst, 2002; de Borst et al., 2004; Jirásek, 2011). Compared to the discrete crack models, the smeared crack models offer the possibility of capturing a large set of complicated cracks in a simplified manner without dealing with many strong discontinuities. However, it has been observed that, when strain softening is considered in a continuum model, numerical results can become highly sensitive to discretization (i.e., the element size in FEM or the nodal distance in meshfree methods). To restore the objectivity of numerical solutions, various regularization methods have been proposed. For instance, the nonlocal regularization methods (Pijaudier-Cabot and Bažant, 1987; Peerlings et al., 1996; Miehe et al., 2010; Ambati et al., 2015; de Borst and Verhoosel, 2016) show promising performance, but these methods require fine meshes in cracking regions, resulting in high computational cost (Heister et al., 2015). Besides, when gradient-type damage models (Peerlings et al., 1996; de Borst et al., 2016) or phase field models (Miehe et al., 2010; Borden et al., 2014; Ambati et al., 2015) are adopted, an additional global equation coupled with the momentum equation needs to be solved for the nonlocal field variables at every time step. Chen et al. (2004) proposed a meshfree formulation to approximate the high-order strain gradients by using implicit gradient reproducing kernel conditions; however, high-order basis functions are required. Other issues with nonlocal models, which deserve further investigation, include the spurious initiation and growth of damage (Simone et al., 2004; Giry et al., 2011; Triantafyllou et al., 2014; Desmorat et al., 2015; Poh and Sun, 2017) and physically unjustified wave dispersion and localization properties of some nonlocal models (Di Luzio and Bažant, 2005; Bažant et al., 2016).

A different remedy to the mesh dependency issue of smeared crack models is based on an appropriate adjustment of the local constitutive law without using nonlocal operators. For example, the crack band approach (Bažant and Oh, 1983; Cervera and Chiumenti, 2006a,b; Jirásek and Bauer, 2012) rescales the post-peak part of the stress–strain law to adjust the bulk energy dissipation of finite elements in order to be consistent with the fracture energy dissipated during the fracturing process. A major advantage of this approach is that the adopted constitutive model remains local (versus the nonlocal theories), which allows the employment of many well-developed constitutive models in a unified manner. Nevertheless, it has been found that the numerical solutions to the standard crack band FEM can still show pathological mesh sensitivity when the mesh is not aligned with the crack propagation direction (Bažant and Lin, 1988; Cervera and Chiumenti, 2006a,b). In addition, the effectiveness of the regularization can be affected by both the finite-element shape and domain integration schemes, and thus it is not always straightforward in ensuring objective energy dissipation (Jirásek and Bauer, 2012).

In the present study, a damage particle method is proposed for fracture modeling under the reproducing kernel approximation and discretization (Liu et al., 1995; Chen et al., 1996, 2017a,b). The smeared strain in the nodal representative domain is defined as the boundary integral of displacements, thus avoiding the need to take direct derivatives of the non-smooth displacement field in the cracking region. The Galerkin approximation of the variational equation is then naturally formulated under the stabilized conforming nodal integration (SCNI) framework (Chen et al., 2001, 2002, 2013), where the field and state variables are computed for the same set of nodes without additional interpolation. This feature allows effective implementation of dissipation energy scaling for each damaged particle such that the bulk energy dissipation over the conforming nodal representative volume is consistent with the surface fracture energy dissipation by the crack segment. Furthermore, the crack path prediction is controlled through the

employment of a simple tracking procedure for damaged particles, which further ensures the objective global energy dissipation, and thus regularizes the numerical solution.

The paper is organized as follows. In Section 2, the continuum damage model and its relation to the cohesive crack model is reviewed and used as the basis for the smeared modeling of brittle fracture. In Section 3, the damage particle method is introduced under a nodally integrated meshfree computational framework, where the smeared strain is defined as the boundary integral of the reproducing kernel approximated displacement field. Furthermore, the scaling of damage laws based on equivalent damage energy and fracture energy dissipations is presented. Numerical examples of benchmark problems are given in Section 4 to examine the effectiveness of this approach, followed by conclusions in Section 5.

## 2. CONTINUUM DAMAGE MODEL

In quasi-brittle materials, the growth and coalescence of a large number of cracks are difficult to capture by discrete crack models. Alternatively, cracked solids can be approximated as damaged continua based on the continuum damage model (CDM), which assumes the following form of the stress–strain relationship:

$$\boldsymbol{\sigma} = (\mathbf{I} - \mathbf{D}) : \bar{\boldsymbol{\sigma}} \quad (1)$$

where  $\mathbf{D}$  is the damage tensor;  $\mathbf{I}$  is the fourth rank identity tensor; and  $\bar{\boldsymbol{\sigma}}$  is the undamaged effective stress tensor. In the present smeared crack approach, the undamaged effective stress is defined as  $\bar{\boldsymbol{\sigma}}(\tilde{\boldsymbol{\varepsilon}}) = \mathbf{C}^e : \tilde{\boldsymbol{\varepsilon}}$ , where  $\mathbf{C}^e$  is the elastic material moduli, and  $\tilde{\boldsymbol{\varepsilon}}$  is the smeared strain, which will be discussed in Section 3. For illustration purposes, an isotropic damage model with  $\mathbf{D} = D(\kappa) \mathbf{I}$  is considered, where the scalar damage variable  $D$  is defined as

$$D(\kappa) = \begin{cases} 0 & \text{for } \kappa < \kappa_0 \\ 1 - \frac{\kappa_0}{\kappa} \frac{\kappa_c - \kappa}{\kappa_c - \kappa_0} & \text{for } \kappa_0 \leq \kappa \leq \kappa_c \\ 1 & \text{for } \kappa_c < \kappa \end{cases} \quad (2)$$

where  $\kappa_0$  is the limit elastic strain under uniaxial tension;  $\kappa_c$  is the critical equivalent strain that controls the slope of the stress–strain softening response; and  $\kappa$  is an irreversible internal state variable, which satisfies the following Kuhn–Tucker conditions:

$$\dot{\kappa} \geq 0 \quad (3)$$

$$\varepsilon_{\text{eq}} - \kappa \leq 0 \quad (4)$$

$$\dot{\kappa} (\varepsilon_{\text{eq}} - \kappa) = 0 \quad (5)$$

Here,  $\varepsilon_{\text{eq}}$  is the equivalent strain (Mazars, 1986)

$$\varepsilon_{\text{eq}} = \sqrt{\sum_{I=1}^3 \langle \varepsilon_I^P \rangle^2} \quad (6)$$

where  $\langle \cdots \rangle$  denotes the Macaulay bracket, and  $\varepsilon_I^P$  is the  $I$ th principal strain.

While the present work focuses on smeared fracture modeling, a comparison between CDM and discrete crack models is essential (Jirásek, 2011; Xu and Waas, 2016). For demonstration purposes, let us consider a model problem that involves the fracturing process of a bar with Young's modulus  $E$ , length  $L$ , and cross-sectional area  $A$  stretched under a displacement control as shown in Fig. 1. The body force and Poisson effects are neglected, and the failure process is triggered by a line of weakened material in the middle of the bar.

Consider a cohesive zone model (CZM) to describe the failure process corresponding to the post-peak stage of the load–displacement response [ $t \geq t_1$  in Fig. 1(d)]. The following linear cohesive traction–separation law is introduced on the cohesive crack surface:

$$\sigma = \left(1 - \frac{w}{w_C}\right) f_t \quad (7)$$

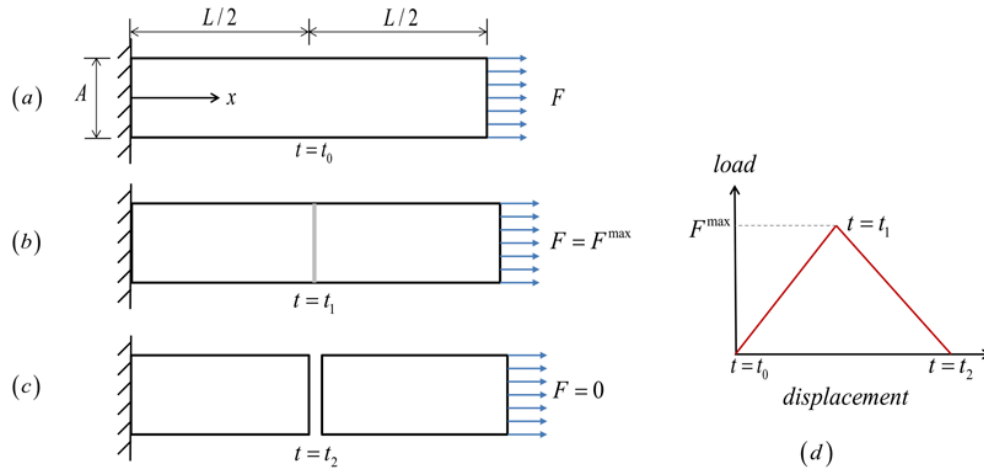


**FIG. 1:** (a)–(c) Illustration of the failure process of a bar with weakened material at the middle cross section; (d) expected load-displacement response

where  $\sigma = F/A$  is the uniaxial stress;  $w = u|_{x=(L/2)^+} - u|_{x=(L/2)^-}$  is the crack opening displacement (COD) at  $x = L/2$  as shown in Fig. 2;  $w_C = (2G_F)/f_t$  is the critical COD ( $G_F$  is the fracture energy); and  $f_t$  is the tensile strength.

The relation between the CZM and the CDM is discussed subsequently, which follows the analogy given in Jirásek (2011). With the cohesive law in Eq. (7), the total displacement  $u_T$  at the loading end of the softening bar is expressed as

$$u_T = u_E + w \quad (8)$$

where  $u_E = \varepsilon_E L = (\sigma/E) L$  denotes the total elastic deformation of the bar, in which  $\varepsilon_E$  denotes the elastic strain. The previous two equations yield the following relationship between the total displacement  $u_T$  and load  $F$  during the failure process:

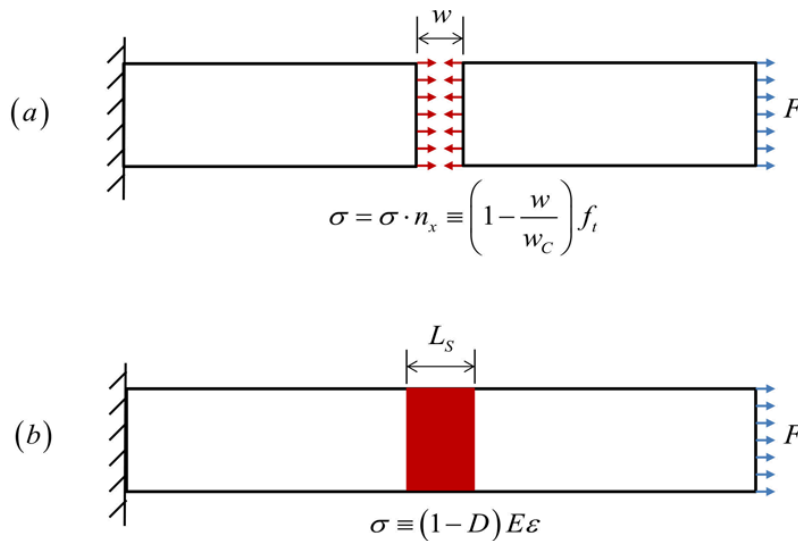


**FIG. 2:** Illustration of adopting the discrete CZM (a) and the CDM (b) for the cracked bar problem

$$u_T = \frac{FL}{EA} + \frac{2G_F}{f_t} \left( 1 - \frac{F}{f_t A} \right) \quad (9)$$

Next, consider the CDM described in Eq. (1), which can be written in the following one-dimensional (1D) form:

$$\sigma = (1 - D) E \varepsilon = E (\varepsilon - D \varepsilon) = E \varepsilon_E \quad (10)$$

From the CDM representation given previously, an inelastic strain  $\varepsilon_C$  can be defined based on an additive decomposition of the total strain  $\varepsilon$  (see the illustration in Fig. 3):

$$\varepsilon = \varepsilon_E + \varepsilon_C \quad (11)$$

where  $\varepsilon_C = D\varepsilon$ . Let the damage zone size be  $L_S$  as shown in Fig. 2(b). The total displacement  $u_T$  of the bar with length  $L$  can be expressed as follows:

$$u_T = \varepsilon_E (L - L_S) + (\varepsilon_E + \varepsilon_C) L_S = \varepsilon_E L + D \varepsilon L_S \quad (12)$$

Comparing Eqs. (8) and (12), it can be seen that the damage model can yield the same load–displacement response as that of the CZM if the following relationship holds:

$$w = D \varepsilon L_S \quad (13)$$

In this connection, the displacement jump  $w$  in the discrete cohesive fracture model has been smeared over the zone with width  $L_S$  in the damage model.

Furthermore, by equalizing the stress generated by the cohesive traction–separation law in Eq. (7) and the damage constitutive law in Eq. (10), and considering Eq. (13), the following expression for the damage evolution can be obtained:

$$D = \frac{1 - (\kappa_0/\varepsilon)}{1 - (\kappa_0 L_S/w_C)} \quad (14)$$

where  $\kappa_0 = f_t/E$  is defined in Eq. (2). The previous equation exactly recovers the damage law defined previously in Eq. (2), if the following condition is satisfied:

$$\kappa_c = w_C/L_S \quad (15)$$

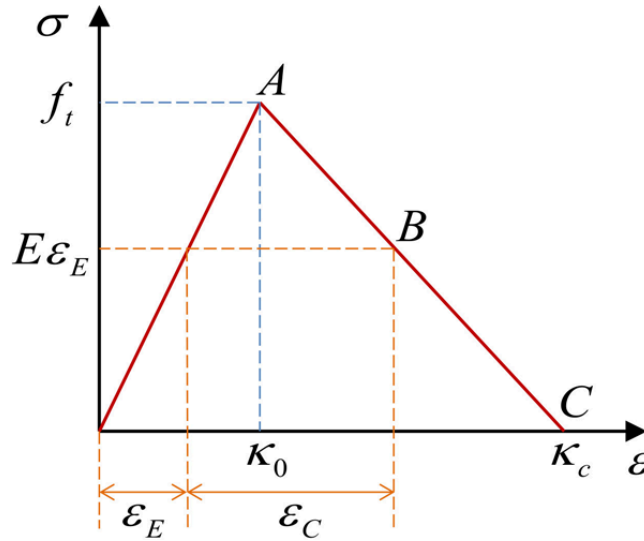


**FIG. 3:** Illustration of the 1D stress–strain relationship based on the CDM, where the tensile strength is reached at point A, complete failure occurs at point C, and point B refers to an arbitrary state at the softening stage

where  $\kappa_c$  is the critical threshold strain. Since  $w_C = (2G_F)/f_t$  represents the critical crack opening, the previous equation implies that  $\kappa_c$  is indeed a model parameter dependent on smeared zone size  $L_S$ . Clearly, treating  $\kappa_c$  as a constant parameter independent of smeared zone size  $L_S$  will lead to an unphysical prediction for this model problem. Computationally, smeared zone size  $L_S$  is related to the adopted discretization grid size, thus a conventional numerical implementation of CDMs results in discretization size dependent, non-convergent solutions. Another computational issue with CDMs for fracture modeling is the spurious prediction of fracture patterns, which tends to appear when the crack propagation path is not aligned with the distribution of the discretization grid. To address the aforementioned issues, a damage particle method is proposed in the next section, where a dissipation energy scaling method is employed in conjunction with the smeared strain formulated under the SCNI framework to achieve a regularized smeared description of fractures.

### 3. THE DAMAGE PARTICLE METHOD

#### 3.1 Reproducing Kernel Approximation

Let us consider a body initially occupying the domain  $\Omega_0$  with the boundary  $\Gamma_0$ , and for a material point  $\mathbf{X} \in \Omega_0$ , where  $\mathbf{x} = \mathbf{x}(\mathbf{X}, t)$  is the position of  $\mathbf{X}$  in the deformed body  $\Omega$  with the boundary  $\Gamma$  at time  $t$ . The variational equation of linear momentum conservation with reference to the current configuration is

$$\int_{\Omega} \rho \delta \mathbf{u} \cdot \ddot{\mathbf{u}} d\Omega + \int_{\Omega} \delta \boldsymbol{\varepsilon} : \boldsymbol{\sigma} d\Omega = \int_{\Omega} \delta \mathbf{u} \cdot \mathbf{b} d\Omega + \int_{\Gamma^h} \delta \mathbf{u} \cdot \mathbf{t} d\Gamma \quad (16)$$

where  $\mathbf{u}$  is the displacement vector;  $\boldsymbol{\varepsilon}$  is the strain tensor;  $\ddot{\mathbf{u}}$  is the acceleration vector;  $\rho$  is the mass density;  $\boldsymbol{\sigma}$  is the Cauchy stress tensor;  $\mathbf{b}$  is the body force vector;  $\mathbf{t}$  is the prescribed traction on the natural boundary  $\Gamma^h$ ; and  $\delta$  denotes the variation. In the following paragraphs, the effects of cracking will be treated with the CDM introduced in Section 2, in conjunction with a regularization scheme to be described in subsequent sections.

The spatial discretization of Eq. (16) is carried out by the reproducing kernel approximation (Liu et al., 1995; Chen et al., 1996), which is constructed based on a set of  $NP$  points  $\{\mathbf{x}_I | \mathbf{x}_I \in \Omega\}_{I=1}^{NP}$ . The reproducing kernel approximation of the displacement field is

$$\mathbf{u}^h(\mathbf{x}, t) = \sum_{I=1}^{NP} N_I(\mathbf{x}) \mathbf{d}_I(t) \quad (17)$$

where  $\mathbf{d}_I(t)$  is the nodal coefficient vector, and  $N_I(\mathbf{x})$  is the reproducing kernel shape function expressed as

$$N_I(\mathbf{x}) = \mathbf{H}^T(0) \mathbf{A}^{-1}(\mathbf{x}) \mathbf{H}(\mathbf{x} - \mathbf{x}_I) \Phi_a(\mathbf{x} - \mathbf{x}_I) \quad (18)$$

in which  $\mathbf{H}(\mathbf{x} - \mathbf{x}_I)$  is a vector consisting of  $n$ th-order monomial basis functions:

$$\mathbf{H}^T(\mathbf{x} - \mathbf{x}_I) = \begin{bmatrix} 1 & x - x_I & y - y_I & z - z_I & (x - x_I)^2 & \cdots & (z - z_I)^n \end{bmatrix} \quad (19)$$

Matrix  $\mathbf{A}(\mathbf{x})$  is called the moment matrix, which is defined as

$$\mathbf{A}(\mathbf{x}) = \sum_{I=1}^{NP} \mathbf{H}(\mathbf{x} - \mathbf{x}_I) \mathbf{H}^T(\mathbf{x} - \mathbf{x}_I) \Phi_a(\mathbf{x} - \mathbf{x}_I) \quad (20)$$

and  $\Phi_a(\mathbf{x} - \mathbf{x}_I)$  is the kernel function that controls the locality and smoothness of the approximation. In this work, the cubic B-spline function is chosen:

$$\Phi_a(\mathbf{x} - \mathbf{x}_I) = \begin{cases} 2/3 - 4s_I^2 + 4s_I^3 & \text{for } 0 \leq s_I \leq 1/2 \\ 4/3 - 4s_I + 4s_I^2 - 4/3s_I^3 & \text{for } 1/2 < s_I \leq 1 \\ 0 & \text{for } s_I > 1 \end{cases}, \quad s_I = \|\mathbf{x} - \mathbf{x}_I\|/a_I \quad (21)$$

where  $a_I$  is the support size of node  $I$ . It can be shown that the reproducing kernel shape function satisfies the following  $n$ th-order discrete reproducing conditions:

$$\sum_{I=1}^{NP} N_I(\mathbf{x}) \mathbf{H}^T(\mathbf{x}_I) = \mathbf{H}^T(\mathbf{x}) \quad (22)$$

More discussions on the mathematical properties of the reproducing kernel approximation and the imposition of essential boundary conditions can be found in Liu et al. (1995) and Chen et al. (1996, 2017a,b).

### 3.2 Approximation of Fracture Surfaces by Damaged Particles

In the present study, the fracture is approximated by a set of discrete crack segments as shown in Fig. 4 in order to circumvent the burden associated with modeling complex crack patterns such as crack branching and coalescence (Remmers et al., 2003; de Borst et al., 2004, 2006; Song and Belytschko, 2009; Rabczuk and Belytschko, 2004, 2007; Rabczuk et al., 2010; Rabczuk, 2013). In contrast to the aforementioned studies, we do not model the crack segments with discrete crack models, which require explicit treatment of discontinuities and singularities. Instead, an attempt is made here to introduce a regularized smeared crack model based on node-based discretization, where the associated nodal representative domains can be generated by the Voronoi diagram as shown in Fig. 4. In each nodal representative domain  $\Omega_L$  associated with  $\mathbf{x}_L$  (Fig. 5), a smeared strain  $\tilde{\epsilon}(\mathbf{x}_L)$  at  $\mathbf{x}_L$  is defined as

$$\tilde{\epsilon}(\mathbf{x}_L) = \frac{1}{V_L} \int_{\Omega_L} \epsilon(\mathbf{x}) d\Omega \quad (23)$$

where  $V_L = \int_{\Omega_L} d\Omega$  is the volume of the nodal representative domain (or area of the nodal representative domain in two dimensions).

Further taking the divergence operation of the smeared strain, we have

$$\tilde{\epsilon}_{ij}(\mathbf{x}_L) = \frac{1}{V_L} \int_{\Omega_L} \epsilon_{ij} d\Omega = \frac{1}{2V_L} \int_{\Omega_L} (u_{i,j} + u_{j,i}) d\Omega = \frac{1}{2V_L} \int_{\Gamma_L} (u_i n_j + u_j n_i) d\Gamma \quad (24)$$

where  $\Gamma_L$  is the boundary of the nodal representative domain  $\Omega_L$ , and  $n_i$  is the  $i$ th component of the outward unit normal to  $\Gamma_L$  as shown in Fig. 5. In the present approach, the smeared strain computed at each nodal representative

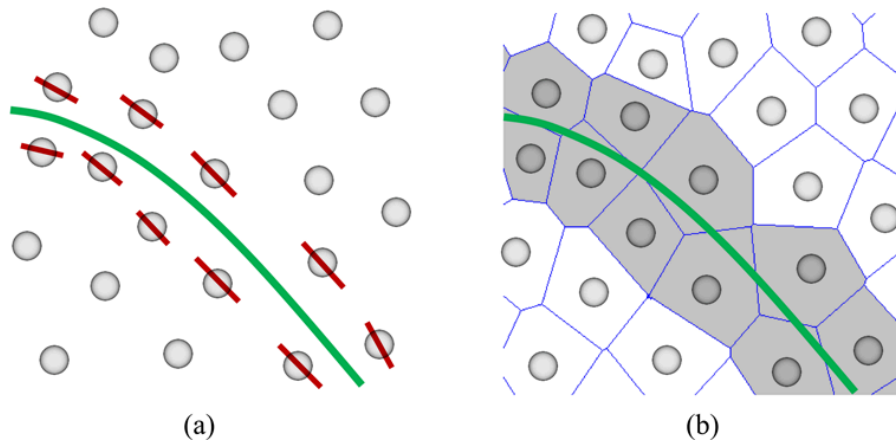


**FIG. 4:** Illustration of the fracture path (long line) and its approximation based on a set of crack segments passing the nodal points of the meshfree model, where the short lines in (a) represent the discrete crack segments and are modeled in a smeared manner over the representative domains in gray associated with damaged particles in (b)

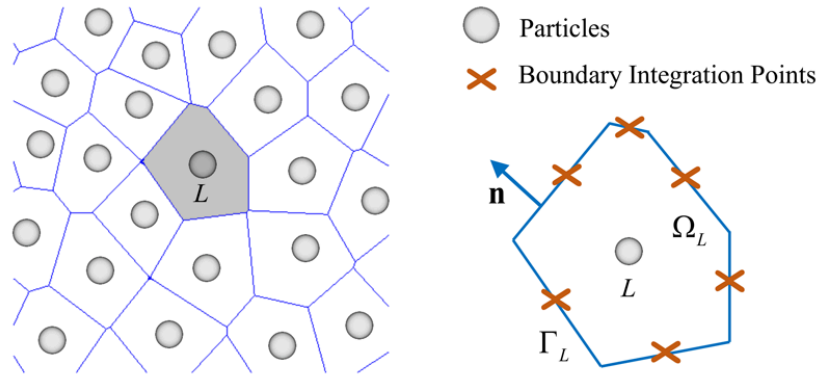


**FIG. 5:** Illustration of the nodal representative domain and boundary integral for smeared strain computation

domain is employed to determine the damage and stress states. For instance, if the CDM in Eq. (1) is considered, then Cauchy stress  $\sigma(\mathbf{x}_L)$  at node  $\mathbf{x}_L$  is computed as

$$\tilde{\sigma}(\mathbf{x}_L) = \{\mathbf{I} - \mathbf{D}[\tilde{\varepsilon}(\mathbf{x}_L)]\} : \bar{\sigma}[\tilde{\varepsilon}(\mathbf{x}_L)] \quad (25)$$

where  $\mathbf{D}[\tilde{\varepsilon}(\mathbf{x}_L)]$  is the damage tensor and  $\bar{\sigma}[\tilde{\varepsilon}(\mathbf{x}_L)]$  is the undamaged effective stress tensor computed based on the smeared strain.

By introducing the reproducing kernel approximation of displacements defined in Eq. (17) into Eq. (24), the following approximated smeared strain  $\tilde{\varepsilon}_{ij}^h(\mathbf{x}_L)$  is obtained:

$$\tilde{\varepsilon}_{ij}^h(\mathbf{x}_L) = \frac{1}{2V_L} \int_{\Gamma_L} (u_i^h n_j + u_j^h n_i) d\Gamma = \frac{1}{2V_L} \sum_{I \in G_L} \int_{\Gamma_L} (N_I n_j d_{iI} + N_I n_i d_{jI}) d\Gamma \quad (26)$$

where  $G_L = \{I | N_I(\mathbf{x}_L) \neq 0\}$  is the set of particles whose associated reproducing kernel shape functions cover particle  $\mathbf{x}_L$ . The resulting form of the smeared strain naturally avoids taking direct derivatives of the displacement field, which is not well-defined near the boundary of the smeared cracking zone. In this work, the boundary integral in Eq. (26) is carried out by one-point integration over the Voronoi cell boundary as shown in Fig. 5, but a higher-order quadrature can be employed if better accuracy is desired.

To capture fracture propagation, we follow the Rankin criterion, which postulates the crack growth direction to be perpendicular to the maximum principal stress direction. To this end, the following criterion (Rabczuk and Belytschko, 2004; Song and Belytschko, 2009) is adopted to identify the candidate damage particles near the predicted crack growth path:

$$\left| \mathbf{n}_L^D \cdot \frac{\mathbf{x}_I - \mathbf{x}_L}{\|\mathbf{x}_I - \mathbf{x}_L\|} \right| = \cos\left(\frac{\pi}{2} - \alpha_{IL}^D\right) < tol \quad \text{for } \mathbf{x}_I \in N_L \quad (27)$$

where  $\mathbf{x}_L$  is the position vector of damaged particle  $L$ ;  $N_L$  is the set containing the neighboring particles of  $\mathbf{x}_L$ , which can be determined by the Voronoi cells;  $\mathbf{n}_L^D$  is the unit normal vector of the crack segment associated with damaged particle  $L$ , which is defined along the maximum principal stress direction at  $\mathbf{x}_L$ ;  $\alpha_{IL}^D$  is the relative angle between the position vector  $\mathbf{x}_I - \mathbf{x}_L$  and the crack segment at damaged particle  $L$ ; and  $tol$  denotes a small tolerance. Criterion (27) is checked at the end of every time step. For example, in the neighbor list of damaged particle  $L$  shown in Fig. 6, only particle  $P$  satisfies this criterion and will be considered as the candidate damage particle for the next time step.

For each candidate damage particle, damage initiation occurs when a certain measure of the smeared strain in nodal representative domain  $\Omega_L$  exceeds a threshold. For example, for the damage law given in Eqs. (2)–(6),  $\varepsilon_{eq}(\tilde{\varepsilon}^h) \geq \kappa_0$  corresponds to the formation of a crack segment. At damage initiation, the unit normal vector  $\mathbf{n}_L^D$  corresponding to the crack segment surface is calculated based on the maximum principal stress direction at particle  $L$  as illustrated in Fig. 6, and is fixed in the subsequent loading process.



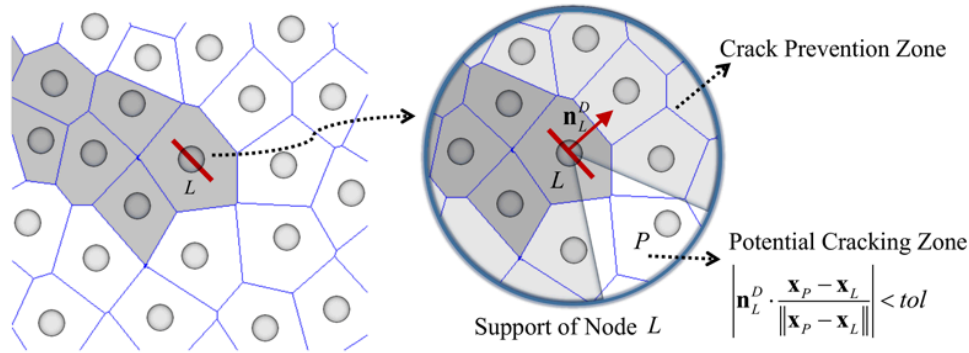


**FIG. 6:** Illustration of the potential cracking zone and the crack prevention zone associated with damaged particle  $L$ , where the short line represents the discrete crack segment located at damaged particle  $L$ , and the representative domains associated with damaged particles are shown in dark gray

### 3.3 Dissipation Energy-based Regularization

Since a set of crack segments is employed to approximate the fracture, the total energy dissipation due to all crack segments is required to satisfy the following condition:

$$\sum_{L \in S_D} (G_F A_L^{\text{eff}}) = G_F A_F \quad (28)$$

where  $G_F$  is the fracture energy dissipated per surface area;  $A_F$  is the fracture surface area (the total length of the long line in Fig. 4);  $A_L^{\text{eff}}$  is the effective surface area of the crack segment associated with damaged particle  $L$ ; and  $S_D$  is the node set that contains all of the damaged particles. Since fracture processes are induced due to the deformation of materials on both sides of the fracture surface as shown in Fig. 4, the geometric relation gives  $\sum_{L \in S_D} A_L \cong 2A_F$ , where  $A_L$  is the area of the intersection plane between the Voronoi cell and the surface perpendicular to the crack normal  $\mathbf{n}_L^D$  at particle  $L$ , as shown in Fig. 7. As such, the effective surface area of the crack segment takes the following relation:

$$A_L^{\text{eff}} = A_L/2 \quad (29)$$

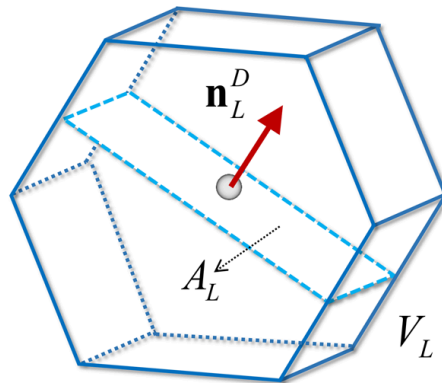


**FIG. 7:** Illustration of the Voronoi cell associated with damaged particle  $L$ , where  $V_L$  is the volume of the nodal representative domain,  $\mathbf{n}_L^D$  is the unit normal vector of the crack segment, and  $A_L$  is the area of the intersection plane between the Voronoi cell and the surface perpendicular to vector  $\mathbf{n}_L^D$  at particle  $L$

Hence, given the geometry of the Voronoi cell and the orientation of the crack segment, the effective surface area  $A_L^{\text{eff}}$  can be calculated and adopted as a geometric approximation to the fracture surface.

To ensure objective energy dissipation in smeared crack modeling, a regularization approach based on the crack band theory (Bažant and Oh, 1983; Cervera and Chiumenti, 2006a,b; Jirásek and Bauer, 2012) is introduced herein. With the CDM, the bulk damage energy dissipation associated with all damaged particles is related to the total surface fracture energy by the following global energy equivalence:

$$\sum_{L \in S_D} g_L V_L = G_F A_F \quad (30)$$

where  $g_L$  is the specific bulk energy dissipation associated with damaged particle  $L$ . To meet the previous requirement, the bulk energy dissipation associated with each damaged particle is made equal to the surface energy required to form a discrete crack segment within the nodal representative domain, that is

$$g_L V_L = G_F A_L^{\text{eff}} \quad (31)$$

With the damage model described in Fig. 3 in Section 2, the specific bulk energy dissipation is expressed as

$$g_L = \frac{1}{2} f_t \kappa_c \quad (32)$$

where  $f_t = E\kappa_0$  is the tensile strength. By substituting Eq. (32) into Eq. (31), the following expression for  $\kappa_c$  is obtained:

$$\kappa_c = \frac{2G_F}{f_t} \left( \frac{A_L^{\text{eff}}}{V_L} \right) = \frac{G_F}{f_t} \left( \frac{A_L}{V_L} \right) \quad (33)$$

When Eq. (33) is adopted to scale parameter  $\kappa_c$ , the corresponding stress–strain softening curve in Fig. 3 is adjusted to ensure energy dissipation equivalence between each damaged particle and the associated crack segment in Eq. (31).

### 3.4 Meshfree Discrete Equations

In the present smeared modeling approach, the domain integration of variational Eq. (16) is performed by SCNI (Chen et al., 2001, 2002) for the following reasons. As has been studied previously, SCNI meets the integration constraints (Chen et al., 2001, 2013) in the Galerkin meshfree approximation of second-order partial differential equations (PDEs) with linear consistency. Moreover, under the SCNI framework the domain is partitioned into conforming nodal representative volumes (e.g., Voronoi cells), such that node-based domain partitioning is provided 1) to compute the smeared strain in Eq. (26) without taking direct derivatives of the displacement field, which are not well-defined in the smeared cracking region; 2) to obtain the effective crack surface area in the smeared crack model in order to transform the fracture energy into damage energy with the aforementioned energy scaling law; and 3) to allow the displacement and damage variables to be computed at the same nodal points without the need of interpolation between variables computed at Gaussian and nodal points in the conventional finite element approaches.

Since the internal energy  $\int_{\Omega} \delta \epsilon : \sigma d\Omega$  in variational Eq. (16) is related to the fracture process of the materials, the nodally integrated discrete form of this internal energy term by the reproducing kernel approximation is subsequently discussed. By introducing a nodal integration, the internal energy  $\int_{\Omega} \delta \epsilon : \sigma d\Omega$  is approximated as follows:

$$\int_{\Omega} \delta \epsilon : \sigma d\Omega \approx \sum_{L=1}^{NP} \delta \tilde{\epsilon}(\mathbf{x}_L) : \sigma[\tilde{\epsilon}(\mathbf{x}_L)] V_L \quad (34)$$

Here,  $\tilde{\epsilon}(\mathbf{x}_L)$  is the smeared strain defined in Eq. (24), and  $V_L$  is the volume (or area in two dimensions) of  $\Omega_L$ . Taking into account the reproducing kernel approximation of the smeared strain in Eq. (26), we have the following approximated smeared stress at  $\mathbf{x}_L$  for the nodal representative domain  $\Omega_L$ :

$$\tilde{\sigma}^h(\mathbf{x}_L) = \sigma[\tilde{\epsilon}^h(\mathbf{x}_L)] = \left\{ \mathbf{I} - \mathbf{D}[\tilde{\epsilon}^h(\mathbf{x}_L)] \right\} : \mathbf{C}^e : \tilde{\epsilon}^h(\mathbf{x}_L) \quad (35)$$

where the damage state  $\mathbf{D}$  within  $\Omega_L$  is determined by the smeared strain  $\tilde{\epsilon}^h(\mathbf{x}_L)$  along with the scaled parameter  $\kappa_c$  based on Eq. (33), which ensures the energy equivalence imposed by Eq. (31) within a nodal representative domain. Note that the nodal volume  $V_L$  and surface area  $A_L$  used in the dissipation energy-based scaling procedure are associated with the same Voronoi cell used for the smeared strain calculation. For convenience, the smeared stress tensor  $\tilde{\sigma}^h(\mathbf{x}_L)$  can be represented in Voigt notation as a vector  $\tilde{\Sigma}(\mathbf{x}_L) = [\tilde{\sigma}_{11}^h(\mathbf{x}_L) \ \tilde{\sigma}_{22}^h(\mathbf{x}_L) \ \tilde{\sigma}_{12}^h(\mathbf{x}_L)]^T$  for two-dimensional problems. Similarly, the vector form of the approximated smeared strain in Eq. (26) can be expressed as follows:

$$[\tilde{\epsilon}_{11}^h(\mathbf{x}_L) \ \tilde{\epsilon}_{22}^h(\mathbf{x}_L) \ 2\tilde{\epsilon}_{12}^h(\mathbf{x}_L)]^T = \sum_{I \in G_L} \tilde{\mathbf{B}}_I(\mathbf{x}_L) \mathbf{d}_I \quad (36)$$

where  $\mathbf{d}_I = [d_{1I} \ d_{2I}]$ , and  $\tilde{\mathbf{B}}_I(\mathbf{x}_L)$  is the associated smeared gradient matrix:

$$\tilde{\mathbf{B}}_I(\mathbf{x}_L) = \begin{bmatrix} \tilde{b}_{1I}(\mathbf{x}_L) & 0 \\ 0 & \tilde{b}_{2I}(\mathbf{x}_L) \\ \tilde{b}_{2I}(\mathbf{x}_L) & \tilde{b}_{1I}(\mathbf{x}_L) \end{bmatrix} \quad (37)$$

$$\tilde{b}_{iI}(\mathbf{x}_L) = \frac{1}{V_L} \int_{\Omega_L} N_{I,i} d\Omega = \frac{1}{V_L} \int_{\Gamma_L} N_I n_i d\Gamma \quad (38)$$

By introducing the reproducing kernel approximation of the smeared strain and smeared stress, the internal force vector  $\mathbf{f}_I^{\text{int}}$  for node  $I$  is computed as follows:

$$\mathbf{f}_I^{\text{int}} \approx \sum_{L=1}^{NP} \tilde{\mathbf{B}}_I^T(\mathbf{x}_L) \tilde{\Sigma}(\mathbf{x}_L) V_L \quad (39)$$

Consequently, the final matrix equations are obtained as follows:

$$\mathbf{M}\ddot{\mathbf{d}} = \mathbf{f}^{\text{ext}} - \mathbf{f}^{\text{int}} \quad (40)$$

where  $\mathbf{M}$  and  $\mathbf{f}^{\text{ext}}$  are the mass matrix and the external force vector, respectively, obtained from variational Eq. (16) by standard procedures (Chen et al., 1996).

*Remark 3.1:* In the proposed method, the computations of the displacement, strain, stress, and damage variables, along with the regularization procedure in Eqs. (31)–(33), are performed at the nodal points. Therefore, this approach avoids the interpolation of state and field variables between the Gaussian and nodal points commonly needed in conventional finite elements, in which the smeared cracking zone size can be affected by the number of Gaussian integration points within each element domain and requires additional treatments (Jirásek and Bauer, 2012).

*Remark 3.2:* The proposed smeared fracture modeling approach naturally fits into the SCNI framework since the proposed smeared strain and the associated nodal integration of internal energy are equivalent to the SCNI framework in Galerkin meshfree methods. As a result, the strain, stress, and variational equations in the undamaged and damaged zones are computed with a unified formulation, where SCNI strain smoothing ensures the accuracy and convergence of the meshfree solutions as analyzed in Chen et al. (2001, 2013).

#### 4. NUMERICAL EXAMPLES

To validate the effectiveness of the proposed formulation, several benchmark fracture problems are analyzed. Linear basis and a cubic B-spline kernel, with a circular nodal support size that is 1.5 times the average nodal distance, are adopted for constructing the reproducing kernel shape functions. The singular kernel method is used for imposition of essential boundary conditions (Chen and Wang, 2000). The diffraction method (Organ et al., 1996) is employed to model pre-existing cracks in the example problems given in Sections 4.2 and 4.3 by modifying the support domain of the nodes, which cover the initial cracks. An implicit incremental–iterative procedure is used for the quasi-static problem in the example given in Section 4.1, and the explicit central difference method is adopted for time integration in the other example problems.

#### 4.1 A Cracked Bar under Tension

Smeared crack approaches provide convenience in fracture modeling since they avoid the complexities associated with explicit modeling of moving strong discontinuities. However, such methods can be ill-posed and lead to discretization-sensitive numerical results, unless effective regularization techniques are employed. To examine the regularization performance of the proposed smeared fracture modeling approach, a fundamental localization test of a bar under uniaxial tension (Jirásek and Bauer, 2012; Xu and Waas, 2016) was analyzed. The damage particle method was employed and the results were compared to that of the CZM as well as the unregularized particle-based damage formulation. Here, the unregularized particle-based damage formulation refers to the damage analysis based on nodally integrated reproducing kernel discretization but without adopting the regularization procedures given in Eqs. (31)–(33), that is, parameter  $\kappa_c$  is kept constant throughout the damage process.

A description of this model problem is given in Section 2 (see Fig. 1). In the investigation, the length of the bar is taken as  $L = 1.0 \times 10^2$  with cross-sectional area  $A = 10.0$  (a dimensionless unit is used). In addition, the bar is considered to be homogeneous with Young's modulus  $E = 2.0 \times 10^6$ , fracture energy  $G_F = 1.885$ , and tensile strength  $f_t = 2.0 \times 10^2$  (i.e., the limit elastic strain of the damage model  $\kappa_0 = f_t/E = 1.0 \times 10^{-4}$ ), except for the weakened material plane at the middle cross section where tensile fracture occurs. To achieve smeared modeling of the fracture process, a slightly lower limit elastic strain of 99.9%  $\kappa_0$  is used for particles whose nodal representative domains intersect with the pre-defined weak plane, such that these particles are damaged once this reduced damage threshold is met. To investigate the solution sensitivity with respect to the discretization size, we adopt four models consisting of 16, 32, 64, and 128 nodes along the rod axis. Accordingly, the fracture at the middle cross section will be captured via damage localization over the nodal representative domains containing the weak plane.

In Fig. 8, the curves of the axial force versus the displacement at the loading end are plotted. It can be seen from Fig. 8(a) that the unregularized particle-based damage formulation suffers from discretization size dependency, i.e., the global energy dissipation (the area under the load–displacement curve) decreases spuriously as the numerical model is refined. This is expected since the specific bulk energy dissipation  $g_I$  is assigned a constant value (i.e.,  $\kappa_c$  is treated as a constant parameter) in the unregularized model, while the volume of the smeared cracking zone (the total nodal representative volume associated with the two damaged particles in this model problem) shrinks as the discretization is refined. The spurious and non-convergent energy dissipation behavior of the unregularized particle-based damage formulation is effectively corrected in the damage particle method [Fig. 8(b)], which ensures that the global energy dissipation is always equivalent to the total fracture energy  $G_F A$  dissipated during the fracturing process through appropriate scaling of the damage law. According to the CZM in Eq. (7), when load  $F$  reduces to zero, the total displacement achieves its maximum magnitude  $u_T^{\max} = 2(G_F A)/F^{\max}$  according to Eq. (9), where  $F^{\max} = f_t A$  is the maximum magnitude of the total force (at the peak of the load–displacement curve). For the

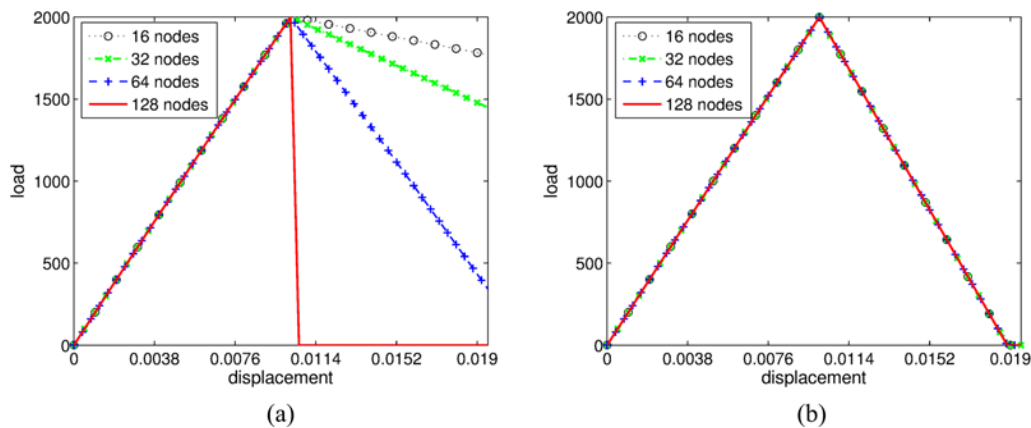


**FIG. 8:** Load–displacement curve obtained from the unregularized particle-based damage formulation (a) and the proposed damage particle method (b)

adopted parameters,  $u_T^{\max} = 1.8850 \times 10^{-2}$  is the expected value, which agrees well with the numerical prediction of  $u_T^{\max} = 1.8858 \times 10^{-2}$  by the damage particle method shown in Fig. 8(b).

Furthermore, the crack opening  $w = \int_{(L-L_S)/2}^{(L+L_S)/2} D \varepsilon dx$  [Eq. (13)] computed from the meshfree simulation is compared to the evolution of the displacement jump  $w$  from the CZM-based analysis in Fig. 9. As expected, the prediction of the damage particle method is consistent with the discrete surface-based cohesive model, while the unregularized formulation suffers from discretization size sensitivity.

At the end of the loading process (i.e., when the displacement at the loading end is equal to  $u_T^{\max}$ ), the predicted maximum magnitude of the damage variable changes as the discretization is refined in the unregularized particle-based damage formulation, as can be seen from Fig. 10(a). For the proposed approach, the damage variable always reaches the maximum value of 1 as shown in Fig. 10(b), which indicates the full opening of the cohesive fracture for all discretizations. Note that the width  $L_S$  of the smeared cracking zone (the region with non-zero damage distribution), defined as the ratio of the nodal representative volume associated with damaged particles to the effective surface area  $A_L^{\text{eff}}$  of the crack segment, decreases with discretization refinement since  $A_L^{\text{eff}} = A/2$  is constant in this model problem. Similar behavior is observed in the crack band FEM when the element size is reduced. However, as discussed in Jirásek and Bauer (2012), the smeared cracking zone width of the crack band FEM can be affected not only by the

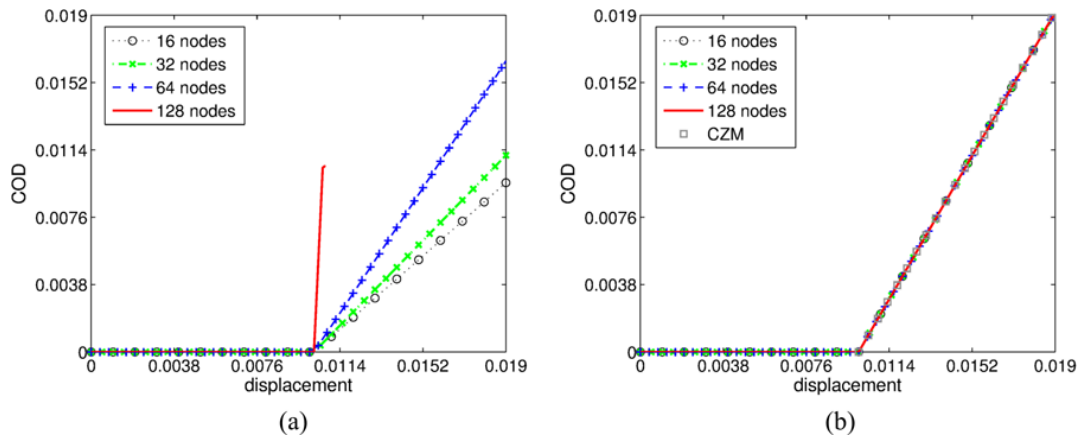


**FIG. 9:** Evolution of COD versus displacement at the loading end of the bar, obtained from the unregularized particle-based damage formulation (a) and the proposed damage particle method (b), where CZM refers to the reference solution based on the CZM

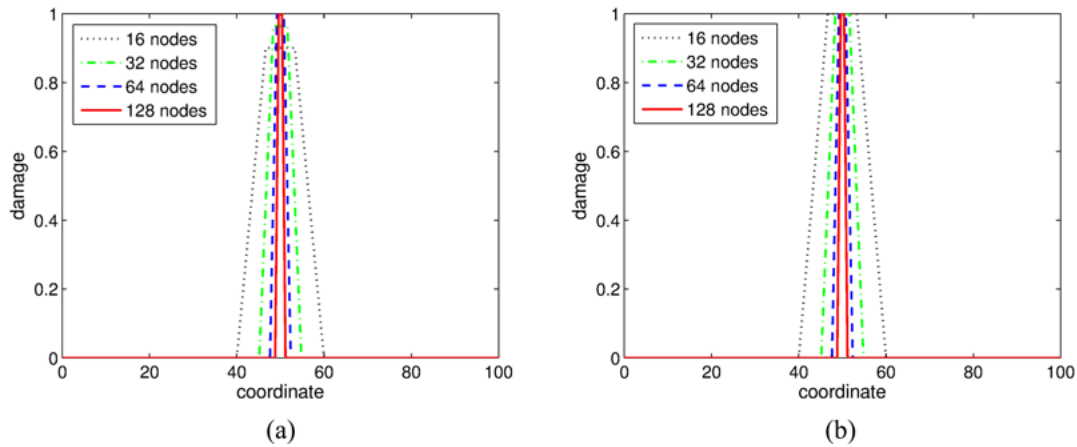


**FIG. 10:** The smeared cracking zone (in terms of non-zero damage distribution along the bar) at tip displacement of  $u_T^{\max}$ , obtained from the unregularized particle-based damage formulation (a) and the proposed damage particle method (b)

element size and shape but also by the integration scheme. This is because softening can localize into only some of the quadrature points within an element, which makes it cumbersome to obtain a reliable estimate of the smeared cracking zone size, especially for multi-dimensional problems. In contrast, since the damage particle method is formulated under the SCNI framework, the smeared zone size can be estimated within each nodal representative domain in a straightforward manner, allowing an effective energy scaling procedure as described in Section 3.

Next, the advantage of employing the smeared strain defined in Eq. (26) in conjunction with SCNI as the domain integration scheme is examined herein. At a time step after damage initiation, the stress distributions obtained from the 8-point Gaussian quadrature and SCNI are plotted in Figs. 11(a) and 11(b), respectively. As shown in Fig. 11(a), when the Gaussian quadrature scheme is used, severe stress oscillations appear and they cannot be eliminated with discretization refinement. This stress prediction could yield spurious damage growth in the subsequent loading steps and cause divergence in the algorithm. Similar stress oscillations were also observed in Jirásek (1998) when the EFG method was adopted to solve a similar strain localization problem. The proposed damage particle method, on the other hand, not only enhances the computational efficiency due to the nodal quadrature nature, but also reproduces the constant stress distribution in Fig. 11(b) as expected, and thus it is well-suited for solving smeared crack problems where localized strain exists. The effectiveness of the proposed damage particle method is attributed to the employment of the smeared strain formulated under the SCNI framework for predicting the stress and damage states, whereas the stress state yielded by the Gaussian quadrature scheme is instead based on the direct derivatives of the non-smooth displacement field, which is not well-defined near the smeared cracking region and thus results in spurious oscillations.

#### 4.2 Kalthoff's Impact Problem

In this example, the fracture behavior of an edge-cracked plate under impulse loading is modeled. At a relatively low impact velocity, brittle failure with a crack propagation angle of about  $70^\circ$  was observed in the experiment as reported in Kalthoff and Winkler (1987). Due to symmetry, only the upper-half of the plate shown in Fig. 12 is considered with edge length  $L_x = L_y = 0.1$  m, and the vertical displacement is restrained on the plane of symmetry. The initial crack length is  $a_1 = 0.05$  m, and the distance from the initial crack to the symmetry plane is  $a_2 = 0.025$  m. An initial velocity of 16.5 m/s in the horizontal direction is introduced on the plate surface where the projectile impacts. The material parameters are as follows: fracture energy  $G_F = 2.0 \times 10^4$  N/m, tensile strength  $f_t = 9.5 \times 10^8$  Pa, Young's modulus  $E = 1.9 \times 10^{11}$  Pa, Poisson's ratio  $\nu = 0.3$ , and mass density  $\rho = 8.0 \times 10^3$  kN/m<sup>3</sup>.

To study the influence of the numerical discretization on the simulation results, models with different levels of discretization refinement are employed. The tolerance in the particle tracking criterion (27) is set as  $tol = 0.3$ .

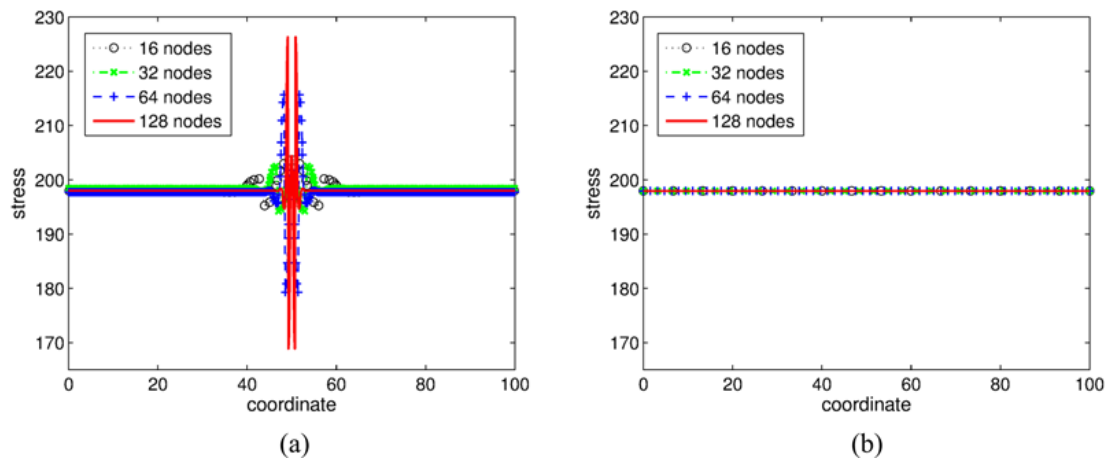


**FIG. 11:** Distribution of axial stress along the bar, predicted by adopting the 8-point Gaussian quadrature using the direct gradient of the displacement field for the strain calculation (a) and the SCNI scheme using the smeared strain (b)

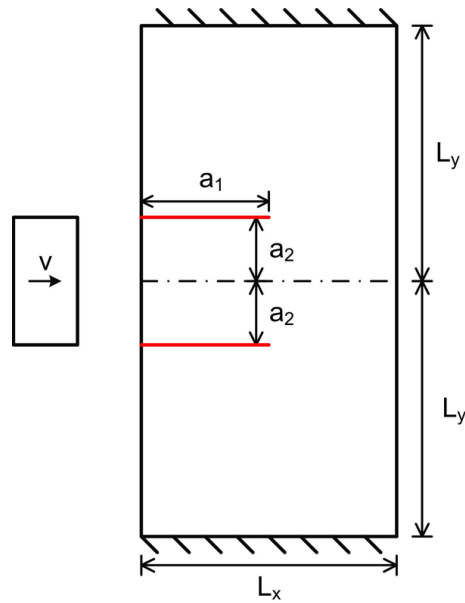


**FIG. 12:** Illustration of Kalthoff's impact problem (the horizontal gray lines represent initial cracks)

This restricts the relative angle  $\alpha_{IL}^D$  in Eq. (27) between the vector  $\mathbf{x}_I - \mathbf{x}_L$  and the crack segment direction to be approximately less than  $20^\circ$ , where  $\mathbf{x}_L$  is the position of the damaged particle and  $\mathbf{x}_I$  is the position of a candidate damage particle. The results of predicted crack paths (shown as damage distribution) are plotted in Fig. 13. It can be seen that consistent crack growth paths are obtained with different refinement levels of the models. Moreover, the predicted crack paths agree well with the reported results using the extended FEM (XFEM) (Rethore et al., 2005), phantom node method (PNM) (Song et al., 2006), cracking node method (CNM) (Song and Belytschko, 2009), and CPM (Rabczuk et al., 2010), as shown in Fig. 14.

In addition to the predicted crack path, the discretization insensitive property of the proposed approach also manifests in the global energy dissipation during the crack growth process. In Fig. 15, the time history of the global energy dissipation of the structure is plotted. Similar to the previous example analyzed in Section 4.1, if the damage evolution law is not scaled properly, the total energy dissipation during the structural failure process decreases as the numerical discretization is refined, as shown in Fig. 15(a). On the other hand, objective energy dissipation is achieved by using the present damage particle method, as shown in Fig. 15(b). The energy dissipation predicted by the CNM in Song and Belytschko (2009) is also plotted in Fig. 15(b) as a reference. In the CNM, discrete crack segments are modeled with the CZM implemented with a partition of unity-based enrichment scheme. Although small discrepancies are observed in the energy dissipation time histories, the overall behaviors predicted by the proposed damage particle method and the CNM agree well.

It is noted that the crack band-type scaling procedure alone is insufficient to fully regularize the solution since the crack path cannot always be predicted correctly without a proper physics-based control. If the particle tracking procedure introduced in Section 3.2 is not employed, the crack pattern in Fig. 16 is obtained. Clearly, spurious damage initiation occurs at locations away from the physical fracture front, and the final crack path prediction is far from satisfactory. Therefore, both the energy scaling and particle tracking procedures are important in achieving objective fracture modeling.

### 4.3 Dynamic Crack Branching Problem

A dynamic crack branching problem is analyzed herein, which remains challenging in finite element-based approaches (Song et al., 2008). As shown in Fig. 17, a plate containing an initial edge crack is subjected to uniform

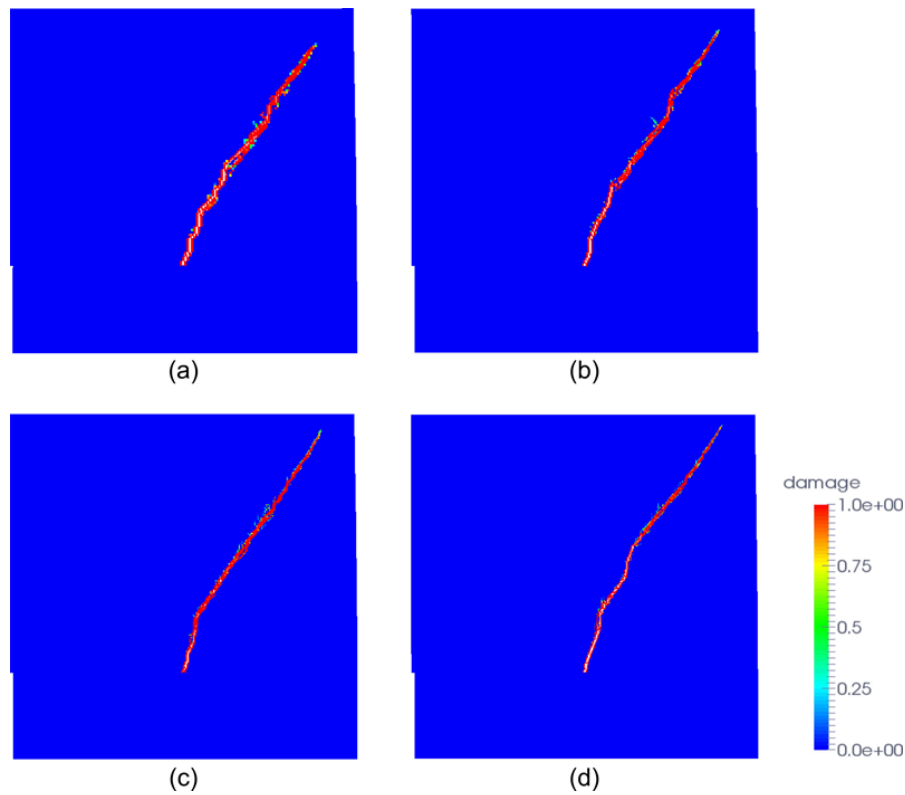


**FIG. 13:** Distribution of the damage state obtained from the damage particle method using 22,500 nodes (a), 62,500 nodes (b), 122,500 nodes (c), and 202,500 nodes (d)

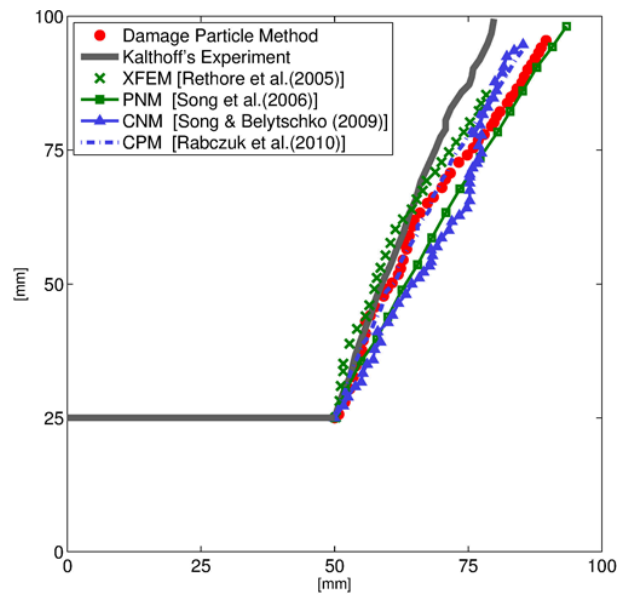


**FIG. 14:** Comparison of the crack growth paths between the Kalthoff's experimental result and different numerical simulations: XFEM (Rethore et al., 2005), PNM (Song et al., 2006), CNM (Song and Belytschko, 2009), CPM (Rabczuk et al., 2010), and the proposed damage particle method



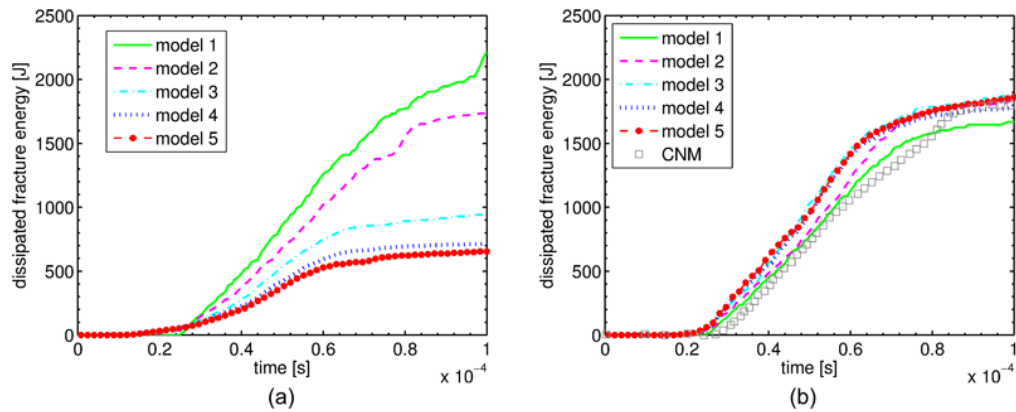


**FIG. 15:** Evolution of global fracture energy dissipation obtained from (a) the unregularized particle-based damage formulation (a), the CNM from Song and Belytschko (2009) (b), and the proposed damage particle method (where model 1 consists of 10,000 nodes; model 2 consists of 22,500 nodes; model 3 consists of 62,500 nodes; model 4 consists of 122,500 nodes; and model 5 consists of 202,500 nodes)

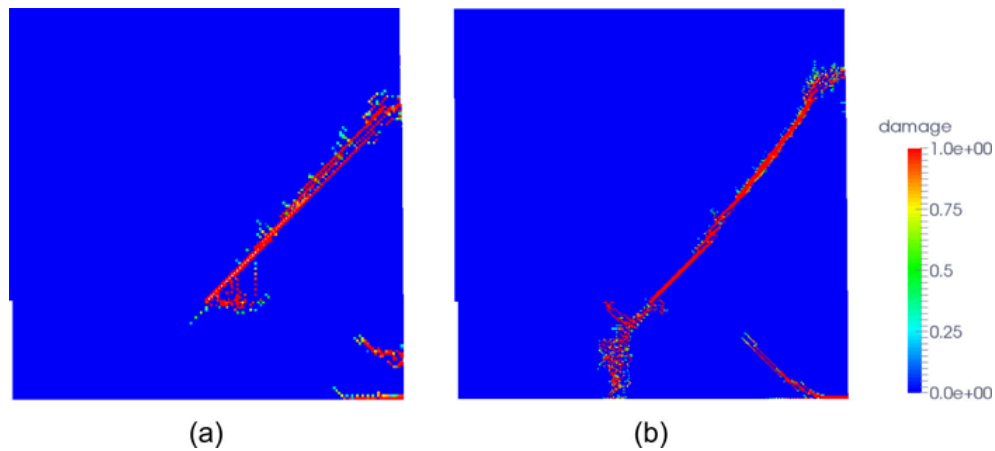


**FIG. 16:** Distribution of the damage state obtained when the damage particle tracking procedure is deactivated using 22,500 nodes (a) and 62,500 nodes (b)

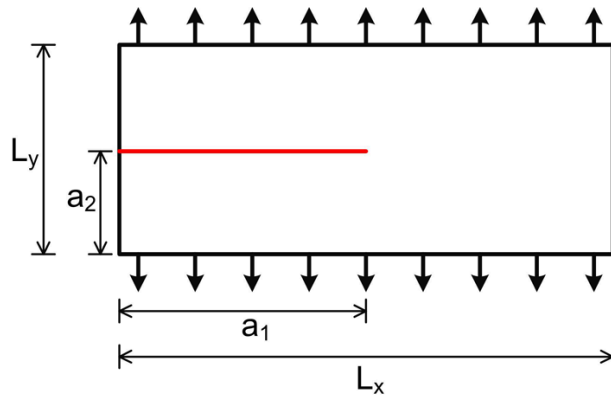


**FIG. 17:** Illustration of the dynamic crack branching problem (the horizontal line represents an initial crack)

tensile tractions of  $1.0 \times 10^6$  Pa on its top and bottom surfaces. The length and width of the plate are  $L_x = 0.1$  m and  $L_y = 0.04$  m, respectively. The initial crack length is  $a_1 = 0.05$  m, and the distance from the initial crack to the bottom edge of the plate is  $a_2 = 0.02$  m. The material parameters are as follows: fracture energy  $G_F = 3.0$  N/m, tensile strength  $f_t = 2.72 \times 10^6$  Pa, Young's modulus  $E = 3.2 \times 10^{10}$  Pa, Poisson's ratio  $\nu = 0.2$ , and mass density  $\rho = 2.45 \times 10^3$  kN/m<sup>3</sup>.

To capture the crack branching phenomena, a relatively large tolerance ( $tol = 0.5$ ) is adopted in the search of potential damage particles, and thus a threshold of  $30^\circ$  for the relative angle  $\alpha_{IL}^D$  in Eq. (27) is introduced. Three levels of refinement with nodal distances  $h = 8 \times 10^{-4}$ ,  $4 \times 10^{-4}$ , and  $2 \times 10^{-4}$  m are adopted in the reproducing kernel discretizations, and the predicted crack paths are shown in Fig. 18. Due to dynamic instability, the crack branches into two major branches, and then a few minor branches also appear along the main branches. Similar crack branching patterns are obtained upon model refinement, and the simulation results agree well with the reported numerical results using the CPM (Rabczuk and Belytschko, 2004, 2007).

Time histories of the global dissipated energy are plotted in Fig. 19. For the damage particle method, convergence in the total energy dissipation is observed when the model is refined as shown in Fig. 19(b), where lower energy

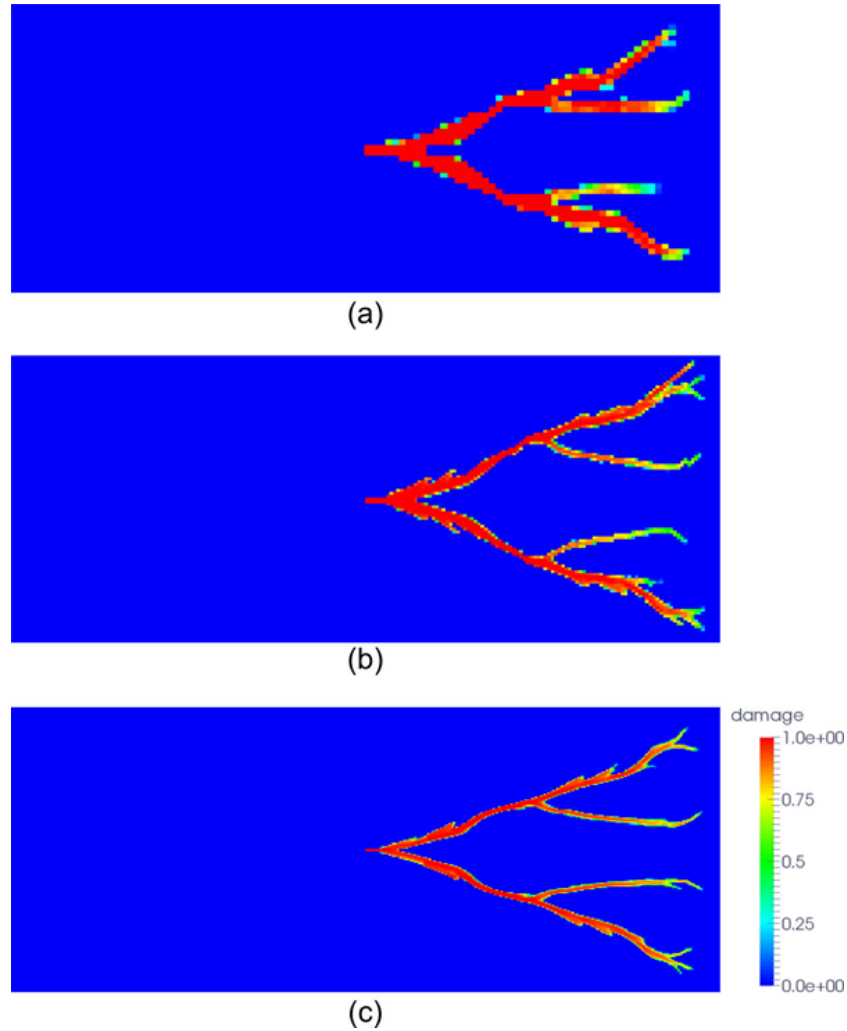


**FIG. 18:** Distribution of the damage state obtained from the damage particle method using different discretizations with the nodal distance: (a)  $h = 8 \times 10^{-4}$  m; (b)  $h = 4 \times 10^{-4}$  m; (c)  $h = 2 \times 10^{-4}$  m

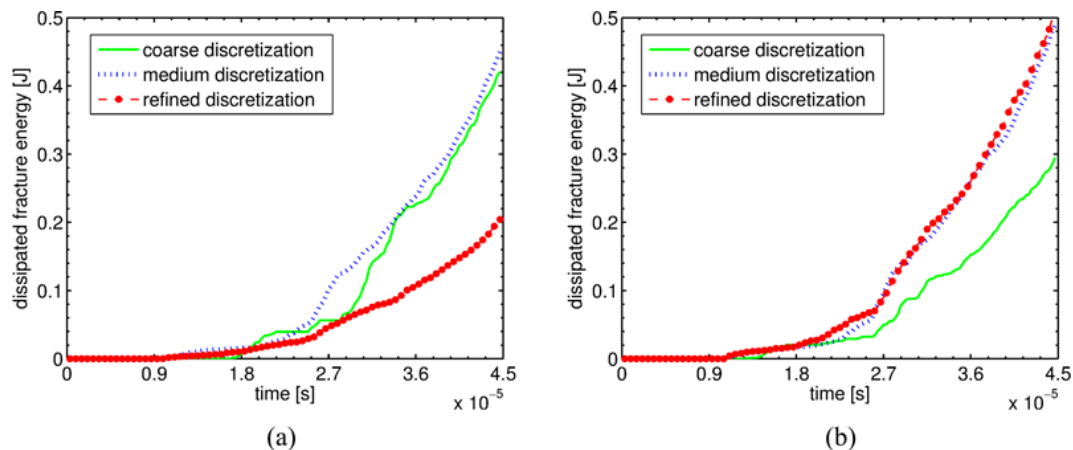


**FIG. 19:** Evolution of global fracture energy dissipation obtained from the unregularized particle-based damage formulation (a) and the proposed damage particle method (b) with different levels of discretization

dissipation with a relatively short crack path [see Fig. 18(a)] appears in the coarsest discretization. However, the total energy dissipation predicted by the unregularized particle-based damage formulation in Fig. 19(a) does not show a convergent behavior upon refinement of the numerical model.

## 5. CONCLUSIONS AND FUTURE WORK

A smeared crack approach for brittle fracture modeling under nodally integrated reproducing kernel discretization has been presented. Since damage is considered as the smeared description of discrete cracks, the smeared strain in a nodal representative domain is defined as the boundary integral of displacements to avoid the ambiguity of taking direct derivatives of non-smooth displacements in the cracking region. With this definition of smeared strain at the nodal representative domain, the SCNI previously proposed for optimal convergence in the Galerkin solution of second-order PDEs with linear consistency can be naturally employed in the damage analysis under a unified framework. In the proposed method, the computation of displacement, strain, stress, and damage variables along with the regularization procedure are all performed at the nodal points. As such, this approach does not require interpolation of state and field variables between the Gaussian and nodal points commonly needed in conventional finite elements. Under this framework, a scaling law is naturally introduced to ensure that the bulk energy dissipated over the nodal representative volume is consistent with the surface fracture energy of the crack segment. Since the present approach is free from mesh entanglement, the energy-based scaling procedure can be performed in a straightforward manner within each nodal representative domain. This is different from conventional crack band FEMs, where the regularization behavior can be affected by both element shapes and integration schemes. Furthermore, spurious damage initiation and spreading is avoided by employing a tracking procedure for damaged particles under the node-based discretization.

The simplicity of the proposed method makes it suitable for capturing multiple propagating fractures. With the unique features of the reproducing kernel approximation, the method can be further extended for modeling extreme deformation problems (e.g., the impact–fragmentation process). In addition, the proposed computational approach can be applied in conjunction with more advanced damage models to consider the effects of anisotropy, plasticity, strain rate, and multiscale phenomena.

## ACKNOWLEDGMENT

The support of this work by the U.S. Army Engineer Research and Development Center under Contract PLA-0009 to UC San Diego is greatly acknowledged.

## REFERENCES

- Ambati, M., Gerasimov, T., and De Lorenzis, L., A Review on Phase-Field Models of Brittle Fracture and a New Fast Hybrid Formulation, *Comput. Mech.*, vol. **55**, no. 2, pp. 383–405, 2015.
- Bažant, Z.P. and Lin, F.B., Nonlocal Smeared Cracking Model for Concrete Fracture, *J. Struct. Eng.*, vol. **114**, no. 11, pp. 2493–2510, 1988.
- Bažant, Z.P., Luo, W., Chau, V.T., and Bessa, M.A., Wave Dispersion and Basic Concepts of Peridynamics Compared to Classical Nonlocal Damage Models, *J. Appl. Mech.*, vol. **83**, no. 11, p. 111004, 2016.
- Bažant, Z.P. and Oh, B.H., Crack Band Theory for Fracture of Concrete, *Mater. Struct.*, vol. **16**, pp. 155–177, 1983.
- Bažant, Z.P. and Pijaudier-Cabot, G., Nonlocal Continuum Damage, Localization Instability and Convergence, *J. Appl. Mech.*, vol. **55**, pp. 287–293, 1988.
- Belytschko, T. and Black, T., Elastic Crack Growth in Finite Elements with Minimal Remeshing, *Int. J. Numer. Methods Eng.*, vol. **45**, no. 5, pp. 601–620, 1999.
- Belytschko, T., Fish, J., and Engelmann, B.E., A Finite Element with Embedded Localization Zones, *Comput. Methods Appl. Mech. Eng.*, vol. **70**, pp. 59–89, 1988.
- Bordas, S., Rabczuk, T., and Zi, G., Three-Dimensional Crack Initiation, Propagation, Branching and Junction in Non-Linear Materials by an Extended Meshfree Method without Asymptotic Enrichment, *Eng. Fract. Mech.*, vol. **75**, no. 5, pp. 943–960, 2008.
- Borden, M.J., Hughes, T.J., Landis, C.M., and Verhoosel, C.V., A Higher-Order Phase-Field Model for Brittle Fracture: Formulation and Analysis within the Isogeometric Analysis Framework, *Comput. Methods Appl. Mech. Eng.*, vol. **273**, pp. 100–118, 2014.
- Cervera, M. and Chiumenti, M., Mesh Objective Tensile Cracking via a Local Continuum Damage Model and a Crack Tracking Technique, *Comput. Methods Appl. Mech. Eng.*, vol. **196**, no. 1, pp. 304–320, 2006a.
- Cervera, M. and Chiumenti, M., Smeared Crack Approach: Back to the Original Track, *Int. J. Numer. Anal. Methods Geomech.*, vol. **30**, no. 12, pp. 1173–1199, 2006b.
- Chen, J.S. and Wang, H.P., New Boundary Condition Treatments in Meshfree Computation of Contact Problems, *Comput. Methods Appl. Mech. Eng.*, vol. **187**, no. 3, pp. 441–468, 2000.
- Chen, J.S., Pan, C., Wu, C.T., and Liu, W.K., Reproducing Kernel Particle Methods for Large Deformation Analysis of Nonlinear Structures, *Comput. Methods Appl. Mech. Eng.*, vol. **139**, no. 1, pp. 195–227, 1996.
- Chen, J.S., Wu, C.T., Yoon, S., and You, Y., A Stabilized Conforming Nodal Integration for Galerkin Meshfree Methods, *Int. J. Numer. Methods Eng.*, vol. **50**, no. 2, pp. 435–466, 2001.
- Chen, J.S., Yoon, S., and Wu, C.T., Non-Linear Version of Stabilized Conforming Nodal Integration for Galerkin Mesh-Free Methods, *Int. J. Numer. Methods Eng.*, vol. **53**, no. 12, pp. 2587–2615, 2002.
- Chen, J.S., Zhang, X., and Belytschko, T., An Implicit Gradient Model by a Reproducing Kernel Strain Regularization in Strain Localization Problems, *Comput. Methods Appl. Mech. Eng.*, vol. **193**, no. 27, pp. 2827–2844, 2004.
- Chen, J.S., Hillman, M., and Rüter, M., An Arbitrary Order Variationally Consistent Integration Method for Galerkin Meshfree Methods, *Int. J. Numer. Methods Eng.*, vol. **95**, no. 5, pp. 387–418, 2013.
- Chen, J.S., Hillman, M., and Chi, S.W., Meshfree Methods: Progress Made after 20 Years, *J. Eng. Mech.*, vol. **143**, no. 4, p. 04017001, 2017a.
- Chen, J.S., Liu, W.K., Hillman, M., Chi, S.W., Lian, Y., and Bessa, M.A., Reproducing Kernel Approximation and Discretization, in *Encyclopedia of Computational Mechanics*, 2nd ed., E. Stein, R. de Borst, and T.J.R. Hughes, Eds., United States: John Wiley & Sons, Ltd., pp. 1–41, 2017b.
- de Borst, R., Fracture in Quasi-Brittle Materials: A Review of Continuum Damage-based Approaches, *Eng. Fract. Mech.*, vol. **69**, no. 2, pp. 95–112, 2002.
- de Borst, R., Remmers, J.J.C., and Needleman, A., Mesh-Independent Discrete Numerical Representations of Cohesive-Zone Models, *Eng. Fract. Mech.*, vol. **73**, pp. 160–177, 2006.
- de Borst, R., Remmers, J.J.C., Needleman, A., and Abellan, M.A., Discrete vs. Smeared Crack Models for Concrete Fracture: Bridging the Gap, *Int. J. Numer. Anal. Methods Geomech.*, vol. **28**, nos. 7–8, pp. 583–607, 2004.

- de Borst, R. and Verhoosel, C.V., Gradient Damage vs Phase-Field Approaches for Fracture: Similarities and Differences, *Comput. Methods Appl. Mech. Eng.*, vol. **312**, pp. 78–94, 2016.
- de Vree, J.H.P., Brekelmans, W.A.M., and Gils, M.A.J., Comparison of Nonlocal Approaches in Continuum Damage Mechanics, *Comput. Struct.*, vol. **55**, pp. 581–588, 1995.
- Desmorat, R., Gatuingt, F., and Jirásek, M., Nonlocal Models with Damage-Dependent Interactions Motivated by Internal Time, *Eng. Fract. Mech.*, vol. **142**, pp. 255–275, 2015.
- Di Luzio, G. and Bažant, Z.P., Spectral Analysis of Localization in Nonlocal and Over-Nonlocal Materials with Softening Plasticity or Damage, *Int. J. Solids Struct.*, vol. **42**, no. 23, pp. 6071–6100, 2005.
- Giry, C., Dufour, F., and Mazars, J., Stress-based Nonlocal Damage Model, *Int. J. Solids Struct.*, vol. **48**, no. 25, pp. 3431–3443, 2011.
- Gravouil, A., Moës, N., and Belytschko, T., Non-Planar 3D Crack Growth by the Extended Finite Element and Level Sets—Part II: Level Set Update, *Int. J. Numer. Methods Eng.*, vol. **53**, no. 11, pp. 2569–2586, 2002.
- Heister, T., Wheeler, M.F., and Wick, T., A Primal-Dual Active Set Method and Predictor–Corrector Mesh Adaptivity for Computing Fracture Propagation using a Phase-Field Approach, *Comput. Methods Appl. Mech. Eng.*, vol. **290**, pp. 466–495, 2015.
- Jäger, P., Steinmann, P., and Kuhl, E., On Local Tracking Algorithms for the Simulation of Three-Dimensional Discontinuities, *Comput. Mech.*, vol. **42**, no. 3, pp. 395–406, 2008.
- Jirásek, M., Element-Free Galerkin Method Applied to Strain-Softening Materials, in *Proc. of Computational Modelling of Concrete Structures (EURO-C)*, R. de Borst, N. Bicanic, H. Mang, and G. Meschke, Eds., Rotterdam, Netherlands: Balkema, pp. 311–319, 1998.
- Jirásek, M., Comparative Study on Finite Elements with Embedded Discontinuities, *Comput. Methods Appl. Mech. Eng.*, vol. **188**, pp. 307–330, 2000.
- Jirásek, M., Damage and Smeared Crack Models, in *Numerical Modeling of Concrete Cracking*, Vienna, Austria: Springer, pp. 1–49, 2011.
- Jirásek, M. and Bauer, M., Numerical Aspects of the Crack Band Approach, *Comput. Struct.*, vol. **110**, pp. 60–78, 2012.
- Jirásek, M. and Zimmermann, T., Analysis of Rotating Crack Model, *J. Eng. Mech.*, vol. **124**, no. 8, pp. 842–851, 1998.
- Kalthoff, J.F. and Winkler, S., Failure Mode Transition at High Rates of Shear Loading, in *Proc. of International Conference on Impact Loading and Dynamic Behavior of Materials*, vol. **1**, pp. 185–219, 1987.
- Krysl, P. and Belytschko, T., The Element Free Galerkin Method for Dynamic Propagation of Arbitrary 3-D Cracks, *Int. J. Numer. Methods Eng.*, vol. **44**, no. 6, pp. 767–800, 1999.
- Liu, W.K., Jun, S., and Zhang, Y.F., Reproducing Kernel Particle Methods, *Int. J. Numer. Methods Fluids*, vol. **20**, nos. 8-9, pp. 1081–1106, 1995.
- Mazars, J., A Description of Micro- and Macro-Scale Damage of Concrete Structures, *Eng. Fract. Mech.*, vol. **25**, pp. 729–737, 1986.
- Miehe, C., Welschinger, F., and Hofacker, M., Thermodynamically Consistent Phase-Field Models of Fracture: Variational Principles and Multi-Field FE Implementations, *Int. J. Numer. Methods Eng.*, vol. **83**, pp. 1273–1311, 2010.
- Moës, N., Dolbow, J., and Belytschko, T., A Finite Element Method for Crack Growth without Remeshing, *Int. J. Numer. Methods Eng.*, vol. **46**, no. 1, pp. 131–150, 1999.
- Moës, N., Gravouil, A., and Belytschko, T., Non-Planar 3D Crack Growth by the Extended Finite Element and Level Sets—Part I: Mechanical Model, *Int. J. Numer. Methods Eng.*, vol. **53**, no. 11, pp. 2549–2568, 2002.
- Oliver, J., Dias, I.F., and Huespe, A.E., Crack-Path Field and Strain-Injection Techniques in Computational Modeling of Propagating Material Failure, *Comput. Methods Appl. Mech. Eng.*, vol. **274**, pp. 289–348, 2014.
- Organ, D., Fleming, M., Terry, T., and Belytschko, T., Continuous Meshless Approximations for Nonconvex Bodies by Diffraction and Transparency, *Comput. Mech.*, vol. **18**, no. 3, pp. 225–235, 1996.
- Parvaneh, S.M. and Foster, C.D., On Numerical Aspects of Different Updating Schedules for Tracking Fracture Path in Strain Localization Modeling, *Eng. Fract. Mech.*, vol. **152**, pp. 26–57, 2016.
- Peerlings, R.H.J., de Borst, R., Brekelmans, W.A.M., and de Vree, J.H.P., Gradient-Enhanced Damage for Quasi-Brittle Materials, *Int. J. Numer. Methods Eng.*, vol. **39**, pp. 3391–3403, 1996.
- Pijaudier-Cabot, G. and Bažant, Z.P., Nonlocal Damage Theory, *J. Eng. Mech.*, vol. **118**, pp. 1512–1533, 1987.

- Poh, L.H. and Sun, G., Localizing Gradient Damage Model with Decreasing Interactions, *Int. J. Numer. Methods Eng.*, vol. **110**, no. 6, pp. 503–522, 2017.
- Rabczuk, T., Computational Methods for Fracture in Brittle and Quasi-Brittle Solids: State-of-the-Art Review and Future Perspectives, *Appl. Math.*, vol. **2013**, Article ID 849231, 2013.
- Rabczuk, T. and Belytschko, T., Cracking Particles: A Simplified Meshfree Method for Arbitrary Evolving Cracks, *Int. J. Numer. Methods Eng.*, vol. **61**, pp. 2316–2343, 2004.
- Rabczuk, T. and Belytschko, T., A Three-Dimensional Large Deformation Meshfree Method for Arbitrary Evolving Cracks, *Comput. Methods Appl. Mech. Eng.*, vol. **196**, pp. 2777–2799, 2007.
- Rabczuk, T., Zi, G., Bordas, S., and Nguyen-Xuan, H., A Simple and Robust Three-Dimensional Cracking-Particle Method without Enrichment, *Comput. Methods Appl. Mech. Eng.*, vol. **199**, nos. 37–40, pp. 2437–2455, 2010.
- Rangarajan, R., Chiaramonte, M.M., Hunsweck, M.J., Shen, Y., and Lew, A.J., Simulating Curvilinear Crack Propagation in Two Dimensions with Universal Meshes, *Int. J. Numer. Methods Eng.*, vol. **102**, nos. 3–4, pp. 632–670, 2015.
- Remmers, J.J.C., de Borst, R., and Needleman, A., A Cohesive Segments Method for the Simulation of Crack Growth, *Comput. Mech.*, vol. **31**, pp. 69–77, 2003.
- Rethore, J., Gravouil, A., and Combescure, A., An Energy-Conserving Scheme for Dynamic Crack Growth using the Extended Finite Element Method, *Int. J. Numer. Methods Eng.*, vol. **63**, no. 5, pp. 631–659, 2005.
- Simo, J.C., Oliver, J., and Armero, F., An Analysis of Strong Discontinuities Induced by Strain-Softening in Rate-Independent Inelastic Solids, *Int. J. Numer. Methods Eng.*, vol. **12**, pp. 277–296, 1993.
- Simone, A., Askes, H., and Sluys, L.J., Incorrect Initiation and Propagation of Failure in Non-Local and Gradient-Enhanced Media, *Int. J. Solids Struct.*, vol. **41**, no. 2, pp. 351–363, 2004.
- Song, J.H., Areias, P., and Belytschko, T., A Method for Dynamic Crack and Shear Band Propagation with Phantom Nodes, *Int. J. Numer. Methods Eng.*, vol. **67**, no. 6, pp. 868–893, 2006.
- Song, J.H. and Belytschko, T., Cracking Node Method for Dynamic Fracture with Finite Elements, *Int. J. Numer. Methods Eng.*, vol. **77**, no. 3, pp. 360–385, 2009.
- Song, J.H., Wang, H., and Belytschko, T., A Comparative Study on Finite Element Methods for Dynamic Fracture, *Comput. Mech.*, vol. **42**, no. 2, pp. 239–250, 2008.
- Swenson, D.V. and Ingraffea, A.R., Modelling Mixed-Mode Dynamic Crack Propagation using Finite Elements: Theory and Applications, *Comput. Mech.*, vol. **3**, pp. 187–192, 1988.
- Triantafyllou, A., Perdikaris, P.C., and Giannakopoulos, A.E., Gradient Elastodamage Model for Quasi-Brittle Materials with an Evolving Internal Length, *J. Eng. Mech.*, vol. **141**, no. 4, p. 04014139, 2014.
- Truster, T.J., On Interface Element Insertion into Three-Dimensional Meshes, *Eng. Fract. Mech.*, vol. **153**, pp. 171–174, 2016.
- Weihe, S., Kröplin, B., and de Borst, R., Classification of Smeared Crack Models based on Material and Structural Properties, *Int. J. Solids Struct.*, vol. **35**, no. 12, pp. 1289–1308, 1998.
- Xu, W. and Waas, A.M., Modeling Damage Growth using the Crack Band Model; Effect of Different Strain Measures, *Eng. Fract. Mech.*, vol. **152**, pp. 126–138, 2016.
- Xu, X.P. and Needleman, A., Numerical Simulation of Fast Crack Growth in Brittle Solids, *J. Mech. Phys. Solids*, vol. **42**, no. 9, pp. 1397–1434, 1994.